# Structural Analyses of Blended Nafion/PVDF Electrospun Nanofibers



| | |
|---|---|
| Journal: | *Physical Chemistry Chemical Physics* |
| Manuscript ID | CP-ART-04-2019-001891.R1 |
| Article Type: | Paper |
| Date Submitted by the Author: | 22-Apr-2019 |
| Complete List of Authors: | Nawn, Graeme; University of Padova, Department of Industrial Engineering, Section of Chemistry for Technology and Energy ; University of Padova, Department of Chemical Sciences<br>Vezzu', Keti; University of Padua, of Industrial Engineering; University of Padua, Chemical Science<br>Negro, Enrico; University of Padova, Department of Chemical Sciences<br>Pace, Guiseppe; Università degli Studi di Padova, Dipartimento di Scienze Chimiche<br>Park, Jun Woo; Vanderbilt, Department of Chemical and Biomolecular Engineering<br>Wycisk, Ryszard; Vanderbilt University, Department of Chemical and Biomolecular Engineering<br>Cavinato, Gianni; Dipartimento di Scienze Chimiche,<br>Di Noto, Vito; University of Padova, Industrial Engineering<br>Pintauro, Peter; Vanderbilt University, Chemical and Biomolecular Engineering |
| | |

Physical Research Paper Submitted

to

*Physcial Chemistry Chemical Physics*

for

# *Structural Analyses of Blended Nafion/PVDF Electrospun Nanofibers*

*(revised #3)*

G. Nawn[1], K. Vezzù[1,2], E. Negro[1,3], G. Pace[4], J. W. Park[5], R. Wycisk[5], G. Cavinato[6], P. N. Pintauro[5],V. Di Noto[1,7]

[1] Section of Chemistry for the Technology (ChemTech), Department of Industrial Engineering, University of Padova, Via Marzolo 9, I-35131 Padova (PD), Italy.

[2] Centre for Mechanics of Biological Materials - CMBM, Via Marzolo 9, I-35131 Padova (PD), Italy.

[3] Centro Studi di Economia e Tecnica dell'Energia *"Giorgio Levi Cases"*, Via Marzolo 9, I-35131 Padova (PD), Italy.

[4] CNR-ICMATE, Via Marzolo 1, I-35131 Padova (PD), Italy.

[5] Department of Chemical and Biomolecular Engineering, Vanderbilt University, Nashville, TN 37235.

[6] Department of Chemical Sciences, University of Padova, Via Marzolo 1, I-35131 Padova (PD), Italy

[7] Consorzio Interuniversitario Nazionale per la Scienza e Tecnologia dei Materiali - INSTM, Via Marzolo 1, I-35131 Padova (PD), Italy

*Keywords:* electrospinning, polyvinylidene fluoride, Nafion, nanofibers, polymer blends, composite membrane

**Abstract**

A new type of polymer blend, prepared by electrospinning nanofibers containing the immiscible polymer polyvinylidene fluoride (PVDF, 10 wt%) and Nafion® perfluorosulfonic acid (90 wt%), has been characterized experimentally. The internal nanofiber morphology is unique and unlike a normal blend, with individual phase-separated and randomly distributed fibrils of Nafion and PVDF (~ 2-7 nm in diameter) that are bundled together and aligned in the fiber axis direction (where the fiber diameter is ~ 500 nm). This morphology is retained when fiber mats are hot-pressed into dense films. The physicochemical properties of the electrospun blended fibers are also highly unusual and unanticipated. As shown in this study, each polymer component influences the thermal and structural behavior of the other, especially in the dry state. Thus, dry composite polymer mats and membranes exhibit properties and attributes that are not observed for either pure PVDF or pure Nafion. Experimental results indicate that: (i) PVDF imparts conformational constraints on the polytetrafluoroethylene (PTFE) backbone chains of Nafion, resulting in an increased $2_1$ helical conformation that effects Nafion's water uptake and thermal properties; and (ii) dipole-dipole interactions between PVDF polymer chains and Nafion makes the β-phase polymorph of PVDF much more stable at elevated temperatures. Such *"reciprocal templating"* in electrospun fibers may not be unique to Nafion and PVDF, thus the procedure represents a new method of creating nanostructured multi-component polymer materials with innovative features.

## 1. Introduction

Uncharged polyvinylidene fluoride (PVDF) and perfluorosulfonic acid ionomers, like DuPont's Nafion®, are widely used as membranes or separators and electrode binders in energy conversion and storage devices (*e.g.*, Li-ion batteries, redox flow batteries, and hydrogen/air fuel cells) [1-3]. PVDF has also been extensively studied in electro-mechanical systems (*e.g.*, strain gauges, transducers and actuators), due to its piezoelectric properties [4, 5]. Both polymers exhibit unique nano-morphologies, which translate into desirable properties. For Nafion, segregated hydrophilic and hydrophobic domains in water-equilibrated films lead to a high proton conductivity and membranes with good mechanical properties. In the case of PVDF, proper polymer processing (*e.g.*, mechanical stretching and electrical poling under a strong electric field) creates β-phase domains with a sizeable piezoelectric constant.

Nafion and PVDF have been blended or somehow combined to form permselective high-performance proton-conducting membranes (PEMs) for fuel cells and redox flow battery applications. For example, membranes from solution-cast Nafion/PVDF blends or PVDF fiber-mat-reinforced Nafion were examined for direct methanol fuel cells, where the addition of hydrophobic PVDF provided mechanical strength and reduced unwanted methanol crossover (although there was a loss in proton conductivity due to the presence of uncharged PVDF) [6-9]. Similarly, blended Nafion/PVDF membranes have also been used in Vanadium redox flow batteries (VRFBs), where the addition of PVDF reduced Nafion swelling and raised ion selectivity with an overall improvement in the coulombic efficiency of the flow battery [3]. More recently, Park *et al.* [10], for example, prepared and characterized Nafion/PVDF membranes from dual fiber electrospun nanofiber mats, with two different membrane morphologies, namely: (i) a PVDF fiber

mat surrounded by Nafion ionomer; and (ii) an interconnected Nafion fiber mat network surrounded by PVDF. The latter membrane type worked well in a hydrogen/bromine regenerative fuel cell, where the presence of PVDF minimized unwanted bromine species crossover and improved membrane selectivity (the ratio of proton conductivity to bromine permeability), relative to commercial Nafion films. In a follow-on paper, Park *et al.* [11] showed that one can effectively blend Nafion and PVDF within the same electrospun nanofiber and then transform the fiber mat into a dense film by simultaneous compaction and heating (a *"hot-pressing"* treatment). The method represents an alternative to conventional blended films and dual fiber electrospun composite membranes. In these fiber mats and membranes, PVDF serves two purposes: (i) it is a carrier polymer that is necessary for electrospinning a Nafion dispersion; and (ii) it is a modifier of Nafion's hydrophilic and mechanical properties. The internal morphology of blended fibers was found to be unique, with Nafion and PVDF phase-separated into fibril strands that are aligned in the fiber axis direction. This unusual structure is attributed to high shear mixing at the spinneret tip during electrospinning, extreme fiber jet elongation after ejection from the spinneret, and rapid solvent evaporation from the fiber which freezes the morphology and prevents redistribution/agglomeration of the PVDF and/or Nafion polymers. Membranes made by hot-pressing Nafion/PVDF blended fiber mats out-performed Nafion 212 in a hydrogen/bromine regenerative fuel cell, due to the combined effects of a low area-specific resistance and low bromine species crossover [12].

The purpose of the present paper is to probe the morphology, polymer properties, and inter-polymer interactions of electrospun Nafion/PVDF blended fibers and dense membranes obtained by hot-pressing such fibers. A single composition of 90/10 w/w Nafion/PVDF has been examined

as a representative example of the membranes introduced by Park *et al.* [11]. We studied samples with several other Nafion/PVDF w/w ratios; we chose the present 90/10 w/w Nafion/PVDF composition since it yielded membranes exhibiting: (i) a high concentration of interactions between Nafion and PVDF, allowing us to better reveal the reciprocal effects of the two polymers on one another; and (ii) a remarkable proton conductivity; thus, the samples described in this work are relevant for applications in practical devices such as fuel cells and redox flow batteries. Membranes with different w/w Nafion/PVDF were studied (w/w varied from 80/20 to 40/60). Nevertheless, the details on the results concerning the other membranes with a composition different from 90/10 Nafion/PVDF, are outside of the scope of the present work and will be the subject of a forthcoming paper. A variety of experimental techniques (SEM, TEM, HR-TGA, TMDSC, WAXD, and ATR-FTIR) were employed to study the samples described in this work. In order to elucidate how the reciprocal interactions between the Nafion and PVDF polymeric components are affected by the preparation procedure, the following samples were considered: "$[P/N_{0.9}]^{M}$", as-spun fiber mat including 90/10 w/w Nafion/PVDF; and "$[P/N_{0.9}]^{MM}$", a dense membrane obtained by hot-pressing $[P/N_{0.9}]^{M}$. In order to sort out the impact of electrospinning, $[P/N_{0.9}]^{M}$ and $[P/N_{0.9}]^{MM}$ are compared with a third sample, a solution-cast 90/10 w/w Nafion/PVDF blend membrane labeled "$[P/N_{0.9}]^{C}$". The interactions between Nafion and PVDF polymeric components are also elucidated by comparing $[P/N_{0.9}]^{M}$ and $[P/N_{0.9}]^{MM}$ with the corresponding reference samples that do not include Nafion: "$[P]^{M}$", neat PVDF electrospun fibers; and "$[P]^{MM}$", a PVDF membrane obtained by hot-pressing $[P]^{M}$. A solution-cast Nafion membrane, indicated as "$[N]^{C}$", is finally studied as a benchmark highlighting the properties of the Nafion ionomer used in the preparation of $[P/N_{0.9}]^{M}$, $[P/N_{0.9}]^{MM}$ and $[P/N_{0.9}]^{C}$. The results show that Nafion and PVDF interact with one another in a new and highly unusual manner when they

are electrospun as blended nanofibers. A careful analysis of the electric response and conductivity mechanism of the various PVDF/Nafion materials examined in the present paper ($[P/N_{0.9}]^M$, $[P/N_{0.9}]^{MM}$ and $[P/N_{0.9}]^C$) is reported in a recently submitted companion paper.[13]

## 2. Experimental Section

### *2.1. Preparation of the samples*

#### *2.1.1. Preparation of electrospun $[P/N_{0.9}]^M$ and $[P]^M$ nanofiber mats*

The electrospinning solution to obtain a mat of Nafion/PVDF blended nanofibers (labeled as $[P/N_{0.9}]^M$, see the Introduction section) is prepared as follows: 1100 EW Nafion powder (0.91 mmol·g$^{-1}$ ion exchange capacity (IEC), prepared by drying LIQUION 1115 from Ion Power Inc.) is dissolved in dimethylacetamide (DMAc) to make a 50 wt% solution. PVDF powder (Kynar® HSV900 from Arkema) is dissolved in a 7:3 weight ratio mixture of DMAc:tetrahydrofuran (THF) to make a 12.5 wt% solution. An electrospinning solution with a Nafion/PVDF weight ratio of 90/10 is prepared by mixing the two individual polymer solutions to obtain 38.4 wt% total polymer concentration (34.6 wt% Nafion and 3.8 wt% PVDF). The electrospinning solution to obtain the $[P]^M$ nanofiber mat is 12.5 wt% Kynar HSV900 in a 7:3 weight ratio mixture of DMAc:THF. Nanofiber mats are made using a custom-built electrospinning apparatus, with a rotating drum collector and a single needle spinneret that is placed in a constant humidity environmental chamber. The Nafion/PVDF solution and the PVDF solution are electrospun using the same conditions: T = 23°C, a constant flow rate of 0.25 mL·h$^{-1}$, a fixed relative humidity of 30 ± 2%, an applied voltage of 13 kV and a spinneret-to-collector distance of 8.5 cm. $[P/N_{0.9}]^M$ and $[P]^M$ are annealed at 150°C

for 90 minutes under vacuum, boiled in 1.0 M $H_2SO_4$ for one hour and finally boiled in deionized water for 1 hour, in order to obtain samples where all the ion-exchange sites are protonated.

*2.1.2. Processing of nanofiber mats to obtain $[P/N_{0.9}]^{MM}$ and $[P]^{MM}$ membranes*

The blended single-fiber Nafion/PVDF mat $[P/N_{0.9}]^{M}$ is transformed into the dense and defect-free $[P/N_{0.9}]^{MM}$ membrane (as determined from SEM images and measured transport properties [10-12]) by hot-pressing at 4000 psi and 177°C for 40 seconds. Instead, the PVDF mat $[P]^{M}$ is hot-pressed at 4000 psi and 190°C for 40 seconds to create dense films indicated as $[P]^{MM}$. During this processing step, the samples are rotated 90° three times and hot-pressed to ensure an even compression. $[P/N_{0.9}]^{MM}$ and $[P]^{MM}$ are annealed at 150°C for 90 minutes under vacuum, boiled in 1.0 M $H_2SO_4$ for one hour and finally boiled in deionized water for 1 hour, in order to obtain samples where all the ion-exchange sites are protonated.

*2.1.3. Preparation of $[N]^{C}$ and $[P/N_{0.9}]^{C}$ solution-cast membranes*

Nafion powder is dissolved in DMAc to make a 20 wt% solution, which is then spread onto a glass plate using a doctor blade. The resulting membrane is dried at 70°C for 12 h and annealed at 150°C for 2 h under vacuum, yielding the $[N]^{C}$ sample. Solution-cast Nafion/PVDF blended membrane samples (90 wt% Nafion and 10 wt% Kynar HSA900 PVDF) are prepared using the nanofiber electrospinning solution. The Nafion/PVDF mixture is cast onto a glass plate using a doctor blade, dried at 70°C for 12 h and annealed at 150°C for 90 minutes under vacuum, yielding the $[P/N_{0.9}]^{C}$ sample. $[N]^{C}$ and $[P/N_{0.9}]^{C}$ are finally boiled for 1 hour each in an aqueous 1.0 M $H_2SO_4$ solution and in deionized water in order to obtain samples where all the ion-exchange sites are protonated.

*2.1.4. Preparation of "dry", "wet" and minimally hydrated ($\lambda$ = 2)*

All the *"dry"* samples are obtained by heating under vacuum at ~110°C inside a glove box for a minimum of 12 hours. This treatment is necessary to ensure the complete removal of all the water molecules included in each sample, with a particular reference to those chemically bound with the $-SO_3H$ groups of Nafion [14]. Indeed, even a very small amount of water molecules (*e.g.*, those that remain in the sample upon a treatment in a dry air desiccator, see below) is known to affect strongly the physicochemical properties of PEMs, with a particular reference to vibrational spectra [14] and charge migration properties [15]. During the drying process $[P/N_{0.9}]^{M}$ and $[P/N_{0.9}]^{MM}$ become purple in color. Exposure of these dry *"purple"* samples to ambient air results in their immediate conversion back to white mats and transparent films (see Figure 1). It should be noted that such an extreme drying step was not performed when testing Nafion/PVDF films in Reference 12.

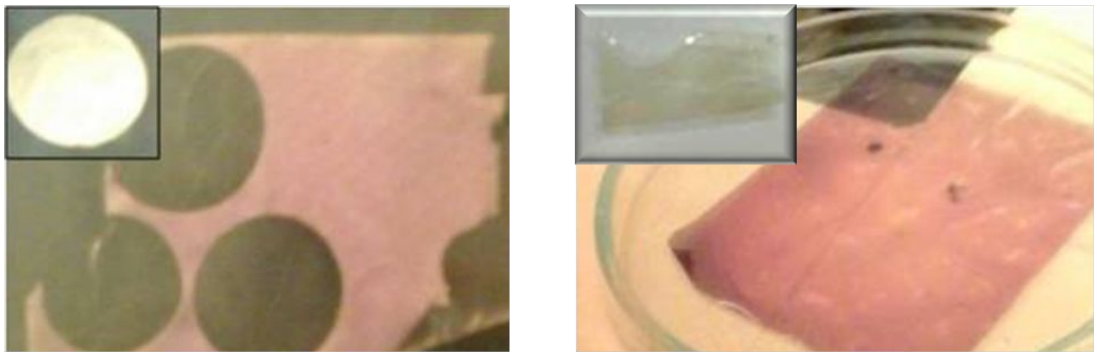

**Figure 1**. Images of $[P/N_{0.9}]^{M}$ (left) and $[P/N_{0.9}]^{MM}$ (right) in the dry state and after exposure to ambient air (insets).

Extensive studies carried out on $[P/N_{0.9}]^{M}$ and $[P/N_{0.9}]^{MM}$ by means of ICP-AES and elemental analysis revealed no impurities (*e.g.*, metals); the observed effect has been tentatively ascribed to a wavelength-dependent scattering phenomenon caused by the morphology of the materials (see Section 3.1). This scattering phenomenon disappears immediately upon introduction of trace amounts of water upon exposure to the atmospheric moisture. Wet samples are prepared by immersion in bidistilled water for 1-10 days at room temperature (for soak times > 1 day, no change in the level of water uptake is observed as gauged by HR-TGA). In addition to producing fully hydrated ($\lambda = 22$) and dry ($\lambda = 0$) $[N]^{C}$ samples (where $\lambda$ is defined as the number of water molecules per sulfonic acid group) [14], Nafion films with residual water content [12], indicated as $[N]^{C}$ ($\lambda = 2$) are prepared as follows. A fully hydrated $[N]^{C}$ ($\lambda = 22$) sample was treated in an autoclave at 121°C for *ca.* 2 hours to erase its thermal history and ensure the reproducibility of its physicochemical properties [16]. Afterwards, the sample was transferred to an ambient temperature dry air desiccator, where it was exposed to a dry air flow for an additional 12 hours. This latter treatment is able to remove most of the water present in the $[N]^{C}$ ($\lambda = 22$) sample with the exception of the few water molecules chemically bound with the $-SO_3H$ groups [14], giving rise to $\lambda = 2$. This value of $\lambda$ was checked by TGA in isothermal desorption mode [17]. The need to obtain a $[N]^{C}$ ($\lambda = 2$) sample stems from comparisons of HR-TGA and ATR-FTIR results of blended fiber samples, as will be discussed below.

*2.2. Instruments and Methods*

High-resolution thermogravimetric analyses (HR-TGA) are carried out using a TGA 2950 thermobalance (TA Instruments) under either nitrogen or dry air flow. The flow rate of either gas during the measurement is set at 100 $cm^3 \cdot min^{-1}$. The sensitivity of the instrument is in the range of

0.1 ÷ 2 %·min$^{-1}$ with a resolution of 1 μg. HR-TGA profiles are collected in the 25 – 950°C temperature range; the heating rate that is varied from 40 to 0.001°C·min$^{-1}$, depending on the first derivative of the weight loss. Approximately 3 mg of sample is loaded onto an open platinum pan. Dry samples are prepared inside a glove box under an argon atmosphere before being transferred quickly to the TGA analyzer, in order to minimize contact with the open atmosphere. In the case of dry samples of $[P/N_{0.9}]^{M}$, $[P/N_{0.9}]^{MM}$ and $[P/N_{0.9}]^{C}$ (that quickly absorb moisture from ambient air, as per Figure 1), the entire analyzer is mounted inside a nitrogen-filled glove bag. Temperature-Modulated Differential Scanning Calorimetry (TMDSC) analyses are performed by means of a DSC Q20 instrument (TA Instruments) equipped with a liquid nitrogen cooling system. Measurements are carried out using a modulated mode over a temperature range between -150 and 350°C, with an effective heating rate of 3°C·min$^{-1}$ and a temperature modulation of ±1.000°C every 60 seconds. Approximately 4 mg of sample is loaded inside a hermetically-sealed aluminum pan. Dry samples are prepared inside a glove box under an argon atmosphere. Attenuated Total Reflectance Fourier Transform Infra Red Spectroscopy (ATR-FTIR) spectra are collected by means of a Nicolet FT-IR Nexus spectrometer with a resolution of 2 cm$^{-1}$. The spectra are obtained with a SPECAC Golden Gate single-bounce diamond ATR accessory in the mid-infrared (MIR) range. Dry samples are prepared inside a glove box under an argon atmosphere. The spectra are obtained by averaging 1000 scans. The baseline correction of the ATR-FTIR profiles is carried out with a Nicolet FT-IR Nexus spectrometer software by setting equal to 0 the intensity of the spectra at 400, 570, 775, 920, 1350, 1480, 2800, 3700 and 4000 cm$^{-1}$. The samples $[P/N_{0.9}]^{M}$, $[P/N_{0.9}]^{MM}$ and $[P/N_{0.9}]^{C}$ are analyzed using transmission electron microscopy (TEM, Philips FEI T12). The samples are embedded in epoxy, cut into 75 nm thick slices with an ultramicrotome (Leica, Ultracut UC7), and then collected on a copper grid. The cutting direction for all the samples is

parallel to the mat/membrane surface. All samples are stained with saturated lead acetate to enhance the contrast between PFSA and PVDF [12]. Wide-angle X-ray diffraction (WAXD) experiments are performed at room temperature using a Scintag XGEN-4000 X-ray diffractometer (ScintagCorp. USA) with a Ni-filtered $CuK_{\alpha}$ radiation source ($\lambda = 0.154$ nm) and with a curved position-sensitive detector (CPS 120).The measurements are carried out in reflection geometry at a scanning rate of $2°\cdot min^{-1}$ over a diffraction angle range of 4° - 60°.

## 3. Results and Discussion

### *3.1. Scanning Electron Microscopy (SEM) and Transmission Electron Microscopy (TEM) analyses*

TEM images (Figure 2) of $[P/N_{0.9}]^{M}$, $[P/N_{0.9}]^{MM}$ and $[P/N_{0.9}]^{C}$ highlight the significant morphological differences that arise as a direct result of the differences in fabrication methods. In $[P/N_{0.9}]^{M}$ the presence of co-aligned polymer fibrils (strands) of width ranging approximately between 2 and 7 nm can be observed within a single fiber (see the inset of Figure 2(a)). Following hot-pressing to obtain $[P/N_{0.9}]^{MM}$, discrete and separated fibers are no longer observed (see Figure 2(b)). Instead, columnar remnants of the parent fibers are present that adopt unusual bundle-type nano-structures of *ca.* 500 nm width. Since the size of these structural domains is comparable to the wavelength of the visible light, it is not to be excluded that that the color of the samples shown in Figure 1 is caused by a wavelength-dependent scattering phenomenon. Bundles of fibrils are positioned in all directions with the column type motifs co-aligned within bundles. For $[P/N_{0.9}]^{C}$, the morphology is very different from that observed in the electrospun composite materials (see

Figure 2(c)). Discrete circular/spherical PVDF domains are present with a diameter of approximately 80 nm. SEM images of $[P/N_{0.9}]^{M}$ show that well-formed fibers of near uniform diameter are produced by electrospinning, with no bead or bead-on-fiber defects (see Figure 2(d)). The fiber mat morphology and interfiber porosity are maintained after thermal annealing, as shown in Figure 2(e), but these features are lost after hot-pressing, where a homogeneously dense and defect-free film (*i.e.*, $[P/N_{0.9}]^{MM}$) is created, as per the top-down membrane view in Figure 2(f).

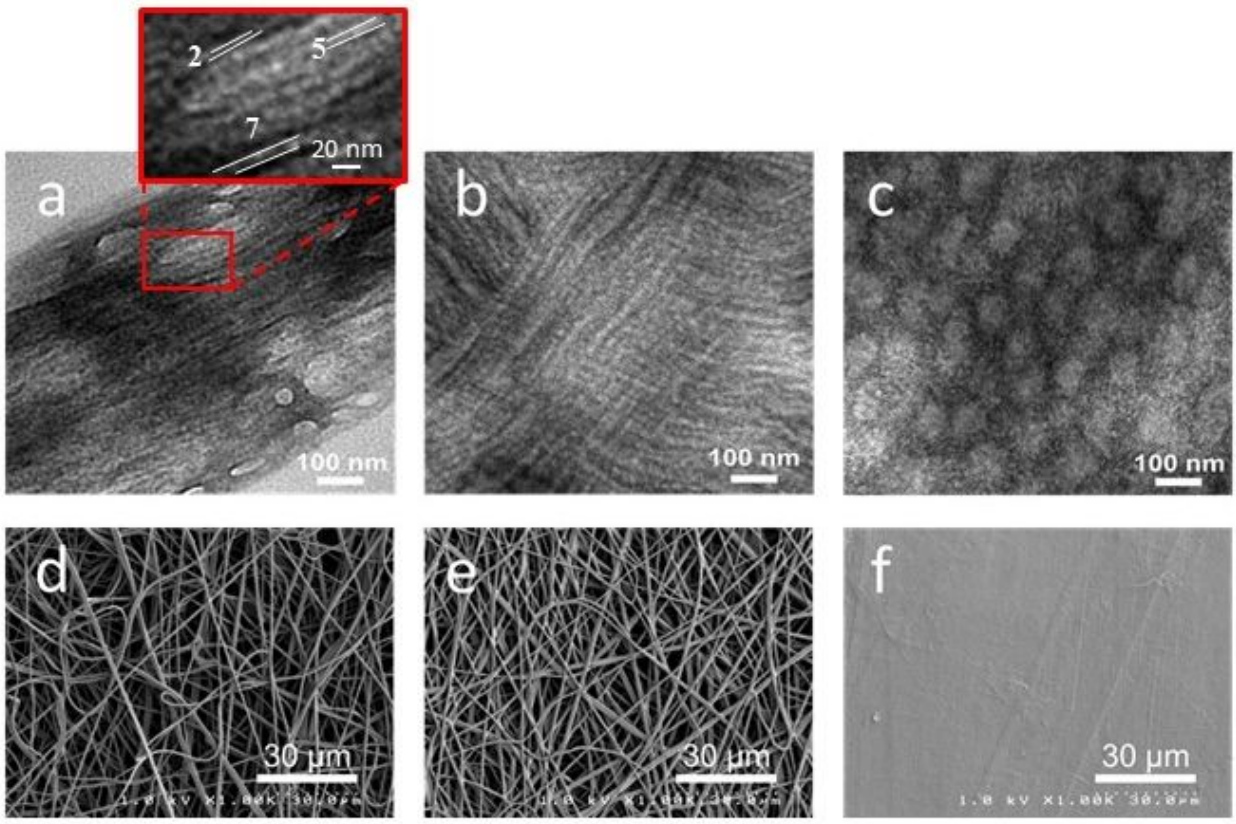


**Figure 2.** TEM images of (a) $[P/N_{0.9}]^{M}$, (b) $[P/N_{0.9}]^{MM}$, (c) and $[P/N_{0.9}]^{C}$. The inset of (a), with its higher magnification, provides additional details on the size of the PVDF fibrils. SEM images of (d) $[P/N_{0.9}]^{M}$, (e) annealed $[P/N_{0.9}]^{M}$ and (f) $[P/N_{0.9}]^{MM}$ (Figures a-c from Reference 12).

*3.2. High-Resolution Thermogravimetric Analysis (HR-TGA)*

The electrospun mat of neat PVDF fibers ($[P]^{M}$) and the dense membrane obtained by hot-pressing the PVDF fiber mat ($[P]^{MM}$) exhibit negligible mass loss up to 160°C, indicative of the hydrophobic nature of the polymer. Both $[P]^{M}$ and $[P]^{MM}$ exhibit high thermal stability with thermal decomposition initiating at temperatures in excess of 450°C [18]. The thermal properties of $[P/N_{0.9}]^{M}$ and $[P/N_{0.9}]^{MM}$ are unsurprisingly similar to those of $[N]^{C}$ (*i.e.*, pristine Nafion), given the fact that the fibers contain 90% Nafion. The thermal profiles of $[P/N_{0.9}]^{M}$ and $[P/N_{0.9}]^{MM}$ are largely equivalent, with thermal stability demonstrated up to *ca.* 190°C. An initial small mass loss (< 160°C) attributed to trace amounts of water is observed, followed by concurrent mass losses attributed to the decomposition of sulfonate groups (I), polyether side chains (II), and finally the fluorocarbon backbone chains (III). A solution cast Nafion/PVDF film ($[P/N_{0.9}]^{C}$) exhibits a slightly enhanced thermal stability, with the onset of decomposition occurring at *ca.* 260°C. This suggests that the fabrication method directly affects the Nafion-PVDF chain interactions (in agreement with the TEM images, see Figure 2), likely by modulating the nature of Nafion domains within the composite materials. The final mass residues observed for $[P/N_{0.9}]^{X}$ (X = M, MM and C) after the HR-TGA experiment are of the expected magnitude (*ca*. 4 w%) given the PVDF content. $[N]^{C}$ ($\lambda = 0$) is thermally stable up to approximately 350°C [19, 20]. The fact that the thermal events for $[P/N_{0.9}]^{X}$ occur at temperatures lower than those observed for a completely dry solution-cast Nafion film (*i.e.*, $[N]^{C}$ ($\lambda = 0$)) suggests that the presence of interchain interactions between PVDF and Nafion influences the thermal behavior of the Nafion component in the blended systems. The result of these interactions is that the Nafion component of $[P/N_{0.9}]^{X}$ does not behave like that of Nafion in $[N]^{C}$ ($\lambda = 0$). It is noteworthy that $[P/N_{0.9}]^{M}$ exhibits an extreme moisture sensitivity. Thus, when exposed to an ambient atmosphere for only a few seconds, an initial mass

loss (attributed to water) of 3 wt% is seen in the HR-TGA profile. This is not observed for either $[P/N_{0.9}]^{MM}$ or $[P/N_{0.9}]^{C}$.

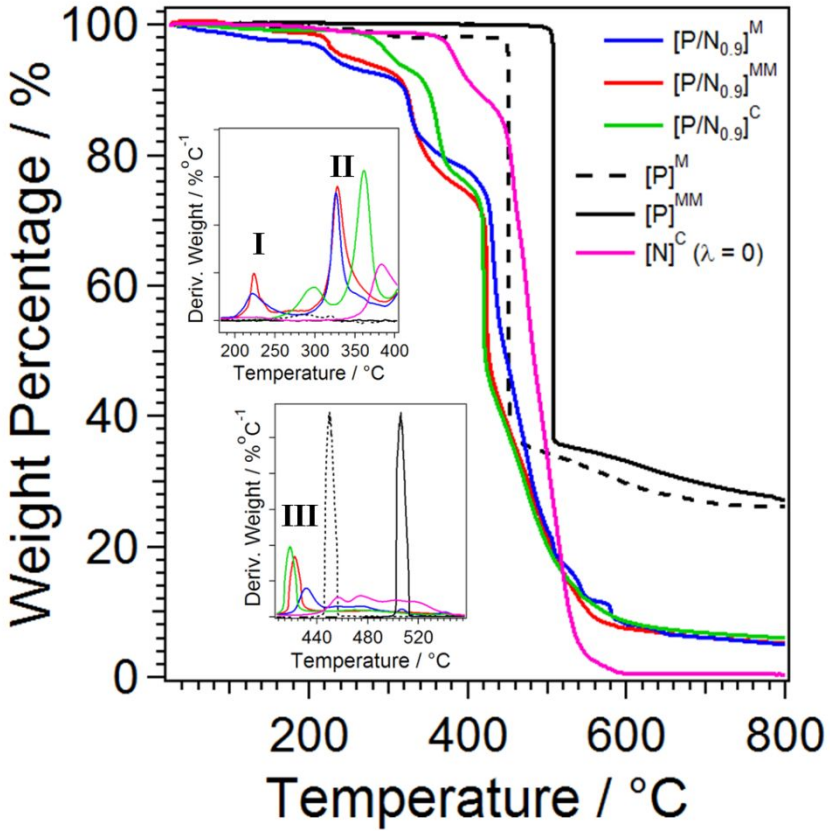


**Figure 3.** HR-TGA of $[P/N_{0.9}]^{M}$ (blue), $[P/N_{0.9}]^{MM}$ (red), $[P/N_{0.9}]^{C}$ (green), $[N]^{C}$ ($\lambda = 0$) (pink), $[P]^{M}$ (black solid) and $[P]^{MM}$ (black dashed) with derivative weights (Deriv.Weight.) (insets). All analyses are conducted under a nitrogen atmosphere with all samples in the dry state (HR-TGA profiles conducted under an air flow can be found in the Supplementary Information Figure SI-1).

After water equilibration,. the same three thermal decompositions (I-III) are observed for $[P/N_{0.9}]^{X}$ (X = M, MM, and C, as per Figure 4). However, water uptake by the composite materials, based on the observed mass loss up to 160°C, is very different from that observed for the liquid water-equilibrated, fully hydrated Nafion sample ($[N]^{C}$ with $\lambda = 22$). $[N]^{C}$ ($\lambda = 22$) displays a water mass

loss of *ca.* 22 wt.%, whereas $[P/N_{0.9}]^{M}$ and $[P/N_{0.9}]^{MM}$ exhibit mass losses of approximately 3 wt.%. Indeed, this lower water content (water loss) is reminiscent of that observed for $[N]^{C}$ ($\lambda = 2$) (*i.e.*, Nafion that has been fully hydrated and then partially dehydrated in a dry air desiccator, see Section 2.1.4.). The restricted water uptake demonstrated by the composite materials, despite the significant water imbibing times (1-10 days), further demonstrates how the presence of PVDF influences the behavior of Nafion. It should also be noted that the water content of the composite films in Figure 4 is lower that that reported in Refence 12, due to the extreme drying step that preceded the water sorption measurements. The onset of thermal degradation for wet $[P/N_{0.9}]^{M}$ and $[P/N_{0.9}]^{MM}$ remains largely unaffected by the presence of water, occurring at temperatures comparable to their dry counterparts. Wet $[P/N_{0.9}]^{C}$ undergoes a slight decrease in thermal stability with respect to its dry analogue, demonstrating a thermal stability comparable to that of wet $[P/N_{0.9}]^{M}$ and wet $[P/N_{0.9}]^{MM}$. It should also be noted that the thermal stability of $[N]^{C}$ ($\lambda = 2$) is also very similar to that of $[P/N_{0.9}]^{M}$ and $[P/N_{0.9}]^{MM}$, unlike in the dry state where the thermal stability of $[N]^{C}$ ($\lambda = 0$) and that of $[P/N_{0.9}]^{X}$ (X = M and MM) are considerably different. It would seem that the interactions between PVDF and Nafion in dry $[P/N_{0.9}]^{M}$ and $[P/N_{0.9}]^{MM}$, which are dipole-dipole in nature, modulate the thermal behavior of the Nafion component in such a way that it does not behave like Nafion ($\lambda = 0$). The presence of water in wet $[P/N_{0.9}]^{M}$ and $[P/N_{0.9}]^{MM}$ disrupts these dipole-dipole interchain forces as they are replaced by hydrogen bonding interactions. This allows the Nafion component within wet $[P/N_{0.9}]^{M}$ and $[P/N_{0.9}]^{MM}$ more freedom to behave like $[N]^{C}$ ($\lambda = 2$), but not the complete freedom to facilitate water uptake to the level of Nafion ($\lambda = 22$).

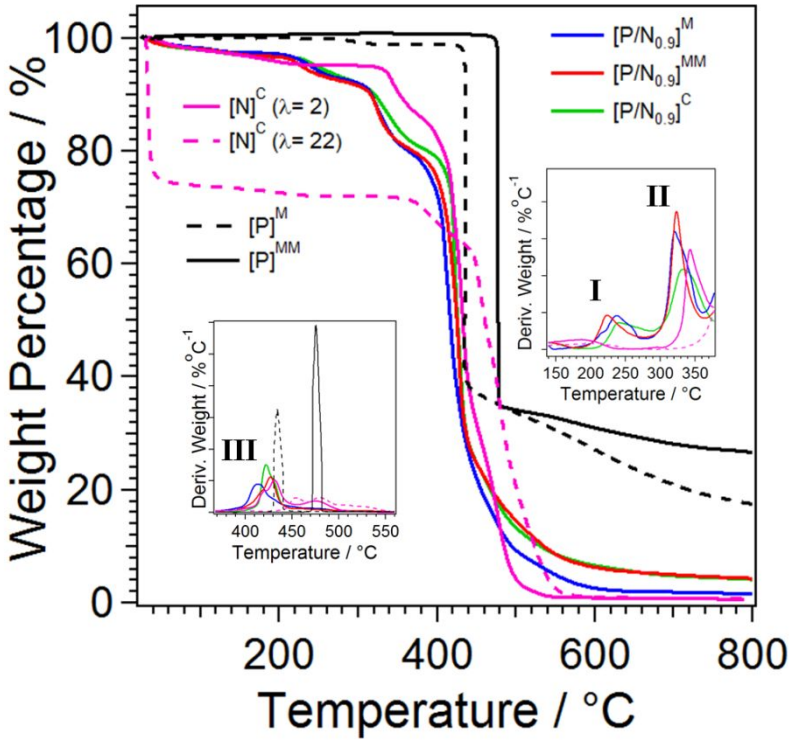


**Figure 4.** HR-TGA of $[P/N_{0.9}]^{M}$ (blue), $[P/N_{0.9}]^{MM}$ (red), $[P/N_{0.9}]^{C}$ (green), $[N]^{C}$ ($\lambda$ = 2) (pink solid), $[N]^{C}$ ($\lambda$ = 22) (pink dashed) $[P]^{M}$ (black solid) and $[P]^{MM}$ (black dashed) with derivative weights (d.W) (insets). All analyses are conducted under a nitrogen atmosphere with all samples in the wet state (HR-TGA profiles conducted under an air flow can be found in the Supplementary Information Figure SI-1).

*3.3. Temperature-Modulated Differential Scanning Calorimetry (TMDSC)*

A complete assignment of the thermal transitions of the pristine homopolymers and polymer blends is carried out by temperature-modulated differential scanning calorimetry (TMDSC). The TMDSC profile of the PVDF fiber mat $[P]^{M}$ exhibits three thermal transitions. A comparison of the total heat flow and of the reversing heat flow profiles highlights the following reversible processes: (i) two order-disorder thermal events located at T ≈ -37 ($T_{gI}$) and T ≈ 84°C ($T_{gII}$); and (ii) a melting event occurring at *ca.* 165°C ($T_{mPVDF}$) (see Figure 5) [4, 5]. In $[P]^{MM}$, $T_{gII}$ undergoes a

shift to a slightly higher temperature ($T \approx 100°C$); however, $T_{gI}$ and $T_{mPVDF}$ are largely unaffected. The morphology resulting after hot-pressing the PVDF mat likely restricts the mobility of the polymer chains; this renders $T_{gII}$ in particular more hindered. In addition, the melting and setting of the PVDF chains during the hot-pressing step results in the formation of microcrystalline domains. The latter are revealed by small shoulders in the TMDSC profiles and are observed at slightly lower temperature than $T_{mPVDF}$. After exposure to water, the thermal transitions of wet $[P]^{M}$ and wet $[P]^{MM}$ are unchanged with respect to the dry state, again reflecting the hydrophobic nature of PVDF that is demonstrated by HR-TGA (see Section 3.2).

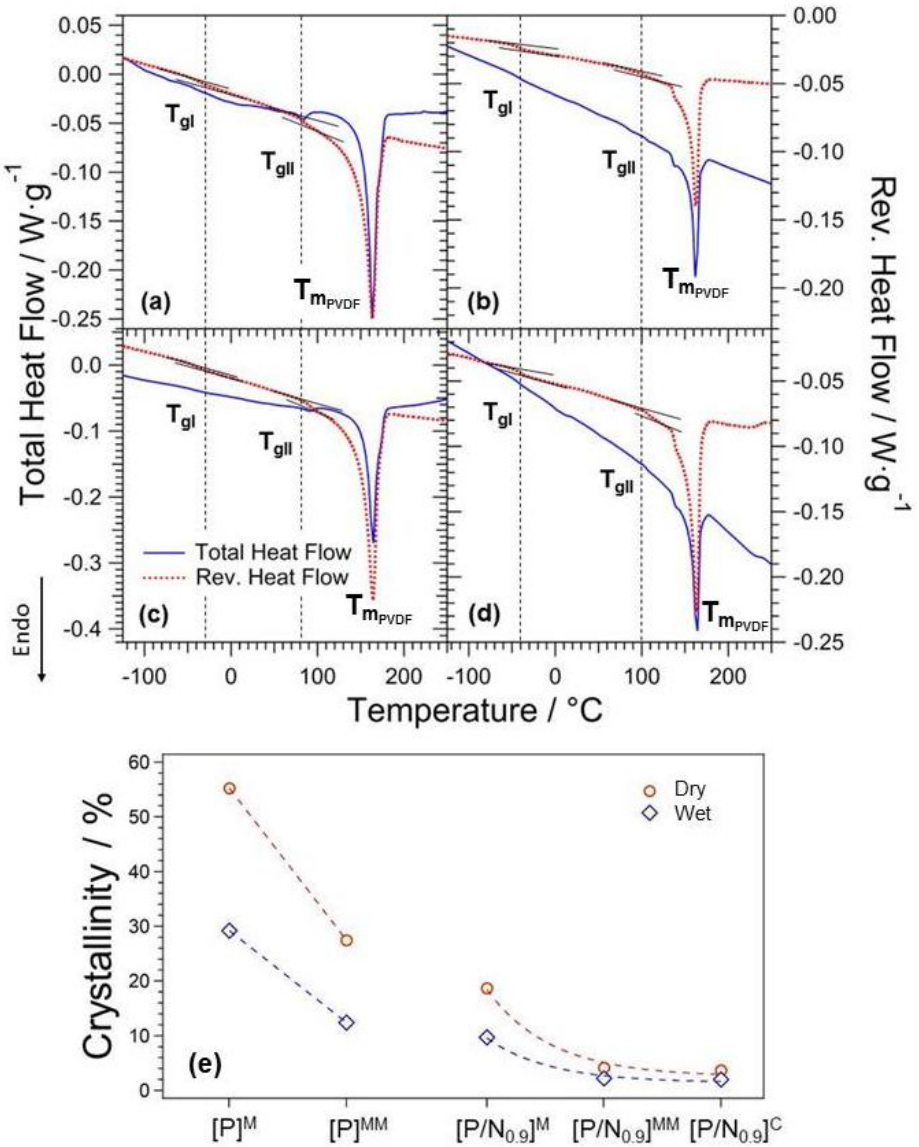


**Figure 5.** TMDSC profile of: (a) dry $[P]^{M}$, (b) wet $[P]^{M}$, (c) dry $[P]^{MM}$ and (d) wet $[P]^{MM}$. Blue and red TMDSC profiles are the total heat flow and the reversing heat flow, respectively. (e) Crystallinity percentage of materials in the dry and the wet state. The crystallinity percentage of the investigated samples is calculated by multiplying by 100 the ratio between: (i) the $\Delta H_i$ of the endothermic peak associated to the melting of PVDF in the TMDSC reversing heat flow profile of the i-th sample; and (ii) the $\Delta H_f$ of the melting of a completely crystalline PVDF sample, where $\Delta H_f = 104.5\ J \cdot g^{-1}$ [21].

The TMSDC profiles of $[N]^C$ exhibit a more dramatic effect with changing hydration level (see Figure 6) [19, 22-25]. The total and reversing heat flow profiles of $[N]^C$ reveal: (i) two reversible glass transition temperatures at $T_{\alpha 1}$ and $T_{\alpha 2}$ and their partially-reversible melting transitions for dry and $\lambda = 2$ membranes, and (ii) two reversible processes ($T_f$ and $T_\delta$) and an irreversible event at $T_{\alpha pc}$ for the wet membrane ($\lambda = 22$). It should be noted that $T_\delta$, which overlaps with the dominating $T_{\alpha pc}$ peak, corresponds to a disorder-order process occurring as polar side chains are interacting by dipole-dipole forces when a weakening of the van der Waals attraction between PTFE backbone chains takes place. This evidence is in accordance with other studies on ionomers [26, 27]. In addition, the most intense $T_{\alpha pc}$ event is a completely irreversible process. Here, for the first time, the analysis of total and reversing heat flow allows us to reveal that the overall transition occurring at 90°C is the superposition of: (i) a reversible disorder-order process ($T_\delta$), which occurs owing to the weakening of the van der Waals attraction between PTFE backbone chains at this temperature and owing to the promotion of stronger dipole-dipole interactions between polar side chains; and (ii) an irreversible $T_{\alpha pc}$ process, which is assigned as described below. The TMDSC profile of $[N]^C$ ($\lambda = 0$) displays an endothermic event at 51°C ($T_{\alpha 1}$), that is attributed to the conformational transition of the backbone chains from the $13_6$ helical conformation to the less constrained $15_7$ conformation [24, 28, 29] (see the WAXD results in Section 3.4 and the ATR-FTIR spectra in Section 3.5 for further discussion on the helical conformations of Nafion). An order-disorder event is also observed at 63°C ($T_{\alpha 2}$), due to the segmental motions of the PTFE backbone chains. Finally, a variety of endothermic events (I-III), associated with the melting of fluorocarbon domains of Nafion and to the degradation of Nafion's $-SO_3H$ fixed charge groups [23] are observed at temperatures above 150°C. The same thermal transitions are observed for $[N]^C$ ($\lambda = 2$), however, they are shifted in

temperature with respect to those of $[N]^C$ ($\lambda = 0$). $T_{\alpha 1}$ decreases in temperature to 25°C, as water facilitates the $13_6$ to $15_7$ conformational transition of Nafion. The opposite effect is observed for $T_{\alpha 2}$, as it increases in temperature to 110°C upon full hydration. A new transition ($T_\beta$) is observed at -37°C, which is attributed to the thermal order-disorder transition of polyether side chains. $T_\beta$ may either be too small or hindered to be observed in the profile of $[N]^C$ ($\lambda = 0$). When $[N]^C$ is fully hydrated ($\lambda = 22$), two major endothermic events are observed: (i) the melting of water domains ($T_f$) at 0°C and the $T_{\alpha pc}$ at 90°C. This latter event is associated with the water-facilitated segmental motions of the backbone and side chains within ionic aggregates [10-12]. Finally, the endothermic events I-III detected for $[N]^C$ ($\lambda = 0$) and $[N]^C$ ($\lambda = 2$) are also revealed for the fully hydrated sample, despite the large and partially overlapping endothermic event peaking at $T_{\alpha pc}$ (see the inset in the bottom panel of Figure 6).

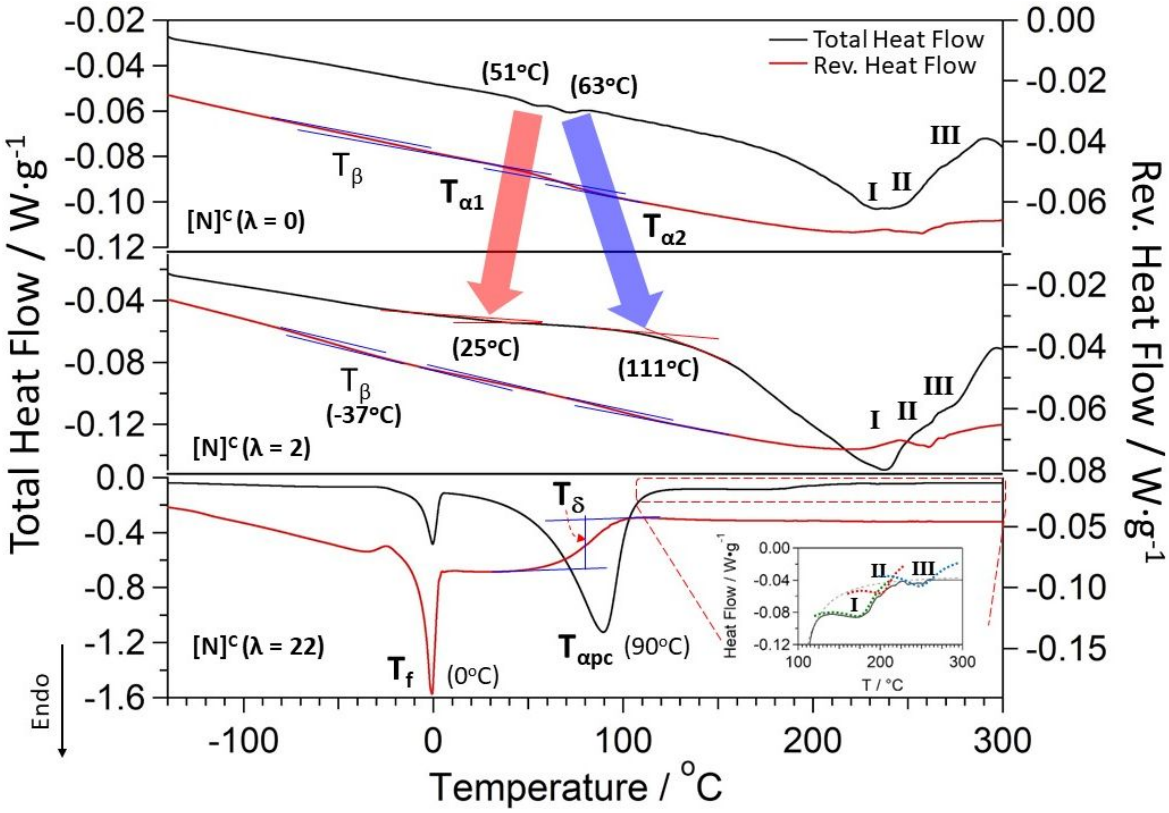


**Figure 6.** TMDSC profile of $[N]^C$ (λ = 0) (top), $[N]^C$ (λ = 2) (middle) and $[N]^C$ (λ = 22) (bottom). Black and red TMDSC profiles are the total heat flow and the reversing heat flow, respectively.

The majority of the following discussion of the thermal transitions of $[P/N_{0.9}]^X$ samples is more easily identified by taking into consideration both the total heat flow and the reversing heat flow of TMDSC profiles (as can be found in the Supplementary Information, Figure SI-2). The low abundance of PVDF in $[P/N_{0.9}]^X$ (X = M, MM or C) renders the order-disorder events that are PVDF-based (*i.e.*, $T_{gI}$ and $T_{gII}$) challenging to observe in the profiles of the composite materials (see Figure 7). Nevertheless. it can be seen that the melting of PVDF ($T_{mPVDF}$) is largely constant between the samples (*ca.* 165°C) regardless of fabrication method (X = M, MM or C) or hydration level (dry *vs.* wet). Nafion-based events are more readily observable, and it is the differences between these events for the composite samples that highlight how the presence of water and the

fabrication method of the blend affect the thermal properties of the final material. For $[P/N_{0.9}]^M$, there are four endothermic events (I-IV) that span the temperature range between 120 and 320°C (with the melting of the nanocrystalline domains accounting for most of these events which occurs at 120 < T < 150°C). This broad temperature range suggests that there is a large size range distribution of PTFE Nafion domains in $[P/N_{0.9}]^M$ [23]. Upon hot-pressing the fiber mat, there is a change in the distribution of these domains, likely as those of smaller size coalesce. Indeed, the resulting TMDSC profile of $[P/N_{0.9}]^{MM}$ displays only one clear melting event (I) at approximately 180°C. A broad halo ascribed to the melting of larger PTFE Nafion domains is revealed at T > 200°C. For $[P/N_{0.9}]^C$ there is once again a broad size distribution of PTFE domains; smaller nanodomains (I) are observed at T < 150°C and larger microdomains at T ≥ 150°C, similar to what is observed in the literature for other Nafion-based systems [23]. The introduction of water into $[P/N_{0.9}]^X$ reduces the density of dipole-dipole interactions between PVDF and the PTFE backbone chains of Nafion and, possibly to some extent, the side chains of Nafion. Consequently, the size of the hydrophobic PTFE domains becomes larger. As a result, the melting events of wet $[P/N_{0.9}]^X$ are rendered quasi-equivalent. Additionally, these events occur at higher temperatures (T > 170°C) with respect to those observed for the dry $[P/N_{0.9}]^X$. Furthermore, the melting events of $[P/N_{0.9}]^X$ (I-IV) are now reminiscent of those observed for $[N]^C$ ($\lambda = 2$).

In the dry state there is little discernible difference in $T_{\alpha 1}$ between all $[P/N_{0.9}]^X$ samples. Indeed, the $T_{\alpha 1}$ of the three $[P/N_{0.9}]^X$ samples is practically the same as that seen in $[N]^C$ ($\lambda = 0$) (see Figure 6 and Figure 7). $T_{\alpha 2}$, however, occurs at higher temperatures for $[P/N_{0.9}]^X$ as compared to $[N]^C$ ($\lambda = 0$). This suggests that in the electrospun and solution-cast composite materials, the PTFE domains of Nafion are stabilized by interactions with PVDF.

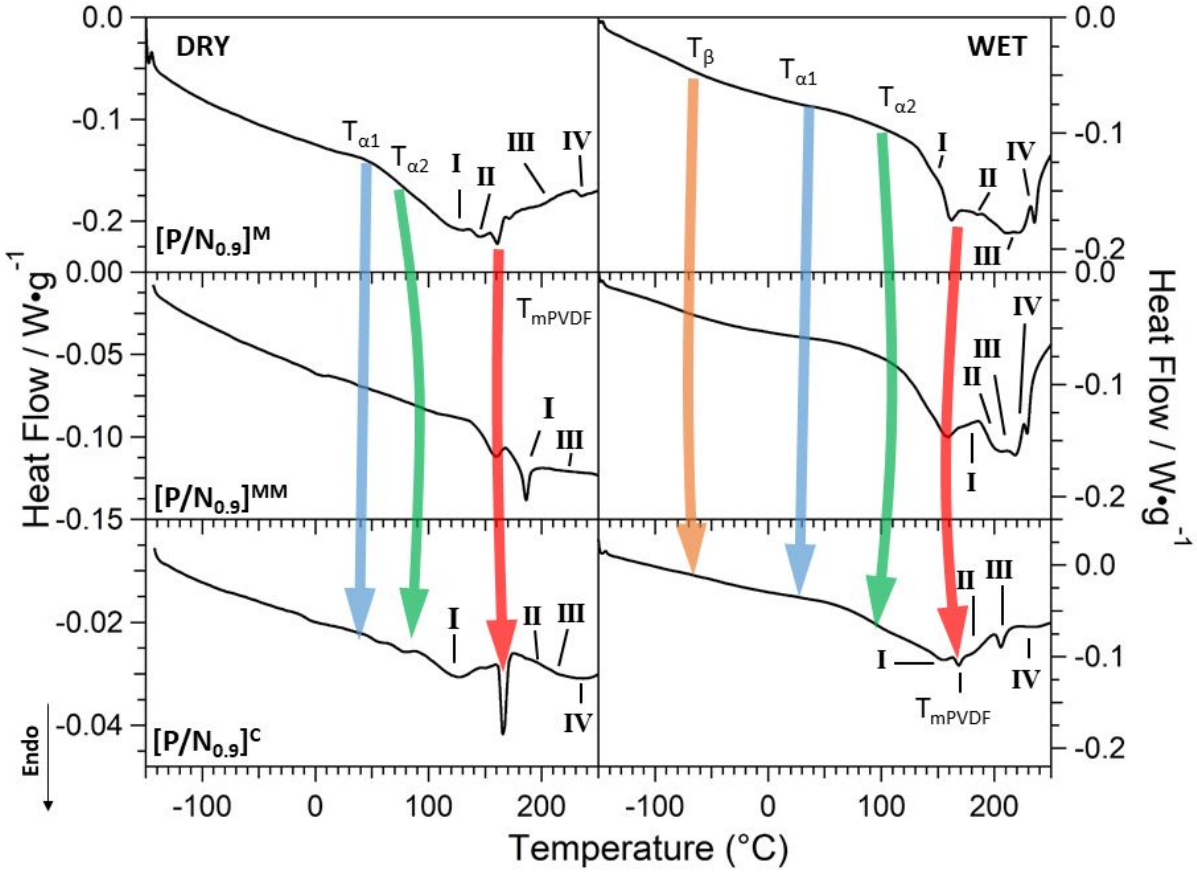


**Figure 7.** TMDSC of $[P/N_{0.9}]^{M}$ (top), $[P/N_{0.9}]^{MM}$ (middle) and $[P/N_{0.9}]^{C}$ (bottom) in dry (left) and wet (right) states. Individual TMDSC profiles can be found in the Supplementary Information Figure SI-2.

Under wet conditions, with respect to the dry analogues ($T_{\alpha1} \approx 45°C$), $T_{\alpha1}$ occurs at a lower temperature for $[P/N_{0.9}]^{X}$ samples ($T_{\alpha1} \approx 30°C$). This temperature difference (*ca.* 15 K), however, is not as large as that observed for $[N]^{C}$ in going from $\lambda = 0$ to $\lambda = 2$. This suggests that the $13_6$ to $15_7$ conformational transition of the Nafion component in $[P/N_{0.9}]^{X}$, although facilitated by water, is not rendered as facile as in $[N]^{C}$ ($\lambda = 2$). $T_{\alpha2}$ occurs at higher temperatures for wet $[P/N_{0.9}]^{X}$ as compared to dry $[P/N_{0.9}]^{X}$ samples (the difference is *ca.* 20 K), with all values of $T_{\alpha2}$ for $[P/N_{0.9}]^{X}$

rendered equal ($T_{\alpha 2} \approx 100°C$) and very similar to that of $[N]^C$ ($\lambda = 2$). This allows us to conclude that the hydrophobic domains of the Nafion component in wet $[P/N_{0.9}]^X$ behave very similarly to those of $[N]^C$ ($\lambda = 2$). $T_\beta$ is clearly observed in wet $[P/N_{0.9}]^X$; again, this event is either hindered or not of sufficient intensity to be observed in the dry derivatives. It is noteworthy that $T_\beta$ in wet $[P/N_{0.9}]^X$ ($\approx$ -65°C) is at a temperature of *ca.* 30 K lower than that for $[N]^C$ ($\lambda = 2$). This may indicate that the interactions between PVDF and Nafion facilitate the order-disorder transition of the polyether side chains of the latter macromolecule. It would seem that for dry $[P/N_{0.9}]^X$, PVDF modulates the nanostructure and the size of PTFE domains of the Nafion so that it does not behave like $[N]^C$ ($\lambda = 0$). However in the wet state, the presence of water facilitates the rearrangements of the PTFE backbone chains, allowing them to behave in a manner similar to $[N]^C$ ($\lambda = 2$). This agrees well with the hydration effect observed by HR-TGA (see Section 3.2). Indeed, even at full hydration, the three $[P/N_{0.9}]^X$ materials never reveal the strong endothermic peaks occurring at $T_f$ and $T_{\alpha pc}$ and displayed by $[N]^C$ ($\lambda = 22$) (see Figure 6, bottom panel). This evidence indicates that the introduction of even a small amount of PVDF (*i.e.*, 10 wt%) in Nafion in $[P/N_{0.9}]^X$ gives rise to interactions that strongly affect the mesoscale structure of the Nafion, decreasing dramatically water uptake by the ionomer. As per the experimental procedures in Reference 12,. If the $[P/N_{0.9}]^X$ materials undergo an extensive purification/hydration procedure in boiling 1M $H_2SO_4$ and water, as per the experimental procedure in Reference 12, and are investigated immediately thereafeer without undergoing the drying process described at the beginning of Section 2.1.4., the morphology/properties are significantly affected, with greater water uptake and a DSC freezing peak for free water. The semiquantitative determination of the crystallinity percentage of PVDF in $[P]^M$, $[P]^{MM}$ and the proposed $[P/N_{0.9}]^X$ materials is determined as described in detail in the caption of Figure 5(e) on the basis of the endothermic event associated with the melting of PVDF,

that peaks at $T_{mPVDF}$. The crystallinity percentages decrease in the order: (i) dry > wet; and (ii) for dry samples, $[P]^{M}$ (55%) > $[P]^{MM}$ (28%) > $[P/N_{0.9}]^{M}$ (22%) > $[P/N_{0.9}]^{MM}$ (4%) ≈ $[P/N_{0.9}]^{C}$ (5%). Wet PVDF samples follow the same trend, but with ~1/2 the crystallinity percentage of their dry counterparts. The crystallinity of PVDF is mostly associated to its β-phase; indeed, the α-phase of PVDF is likely less prone to form crystalline domains in these conditions owing to its alternating, less compact TGTG' conformation (see below in Section 3.4). Taken all together, the results show that: (i) the interactions between Nafion and PVDF act to stabilize the crystalline domains of PVDF in $[P/N_{0.9}]^{X}$; and (ii) the hot-pressing process and the water uptake of the Nafion component both act to reduce the amount of crystallinity of the PVDF component in the materials. These trends are in accordance with the vibrational studies (see Section 3.5), which indicate that the crystallinity percentage is mostly associated with β-phase PVDF. This form of PVDF is highly sensitive to the processing steps and to interactions with the environment.

*3.4. Wide Angle X-ray Scattering (WAXD) Analysis*

PVDF crystallizes in 4 distinct polymorphs, α, β, γ and δ ,with the α- and β-phases (shown in Figure 8) being the most common and readily distinguishable by IR spectroscopy [4, 20]. α-phase PVDF is obtained by crystallization of the melt, resulting in monomers adopting a TGTG' (T = trans, G = gauche) conformation. β-phase PVDF is obtained by mechanical drawing or electric field poling of the α-phase, or alternatively by crystallization from solution. For β-phase PVDF the resulting vinylidene difluoride moieties adopt an all trans zig-zag (TTT) conformation, as shown in Figure 8 [30, 31].

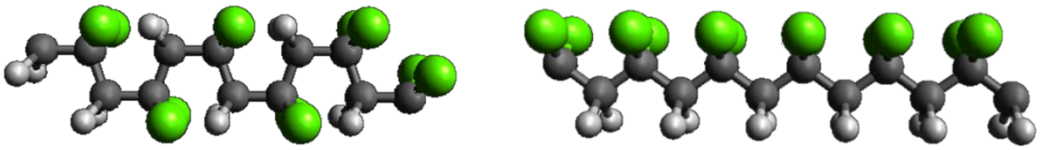

α-PVDF β-PVDF

**Figure 8.** α-phase PVDF in the alternating trans-gauche conformation TGTG' (left) and β-phase PVDF in the trans-trans conformation TTT (right); carbon atoms (grey), hydrogen atoms (white) and fluorine atoms (green).

The conformation of PVDF chains in mats obtained via electrospinning can dramatically vary from preferentially adopting one polymorph, to a combination of polymorphs [32-34]. The PVDF in $[P]^M$ is almost entirely in the β-phase, based on the dominating peak in the WAXD pattern centered at $2\theta = 20.8^o$, and a peak of weak intensity at $2\theta = 36.3^o$ (see Figure 9) [31, 35-38]. There are some minor contributions attributed to the α-phase appearing as a less intense shoulder at lower 2θ of *ca.* $18^o$. The presence of other polymorphs (γ or σ) is not detected in the WAXD pattern. The conformational nature of Nafion (the PTFE component in particular) has been thoroughly investigated and it is widely accepted that the perfluorinated domains can adopt a variety of different helical arrangements, labeled as $2_1$ (alternatively named $13_6$), $10_3$, and $15_7$ [19, 39-48]. The WAXD pattern for recast Nafion ($[N]^C$ with $\lambda = 2$) consists of three peaks; a low intensity very broad signal observed at $2\theta = 39°$, ascribed to the ordering of $CF_2$ units in crystalline hydrophobic PTFE domains, a strong broad peak at $2\theta = 16.1°$ ascribed to non-crystalline PTFE domains, and a sharp medium intensity peak at $2\theta = 17.7°$ ascribed to crystalline PTFE domains. The crystalline region is comprised of the $15_7$ helical conformation with the non-crystalline region attributed to the $10_3$ helical conformation based on ATR-FTIR assignments (see ATR-FTIR section) and

previous studies reported in the literature [40, 41]. The WAXD patterns for $[P/N_{0.9}]^X$ appear to be a superposition of those peaks corresponding to $[N]^C$ ($\lambda = 2$) and $[P]^M$ (taking into account the relative abundances of each component).

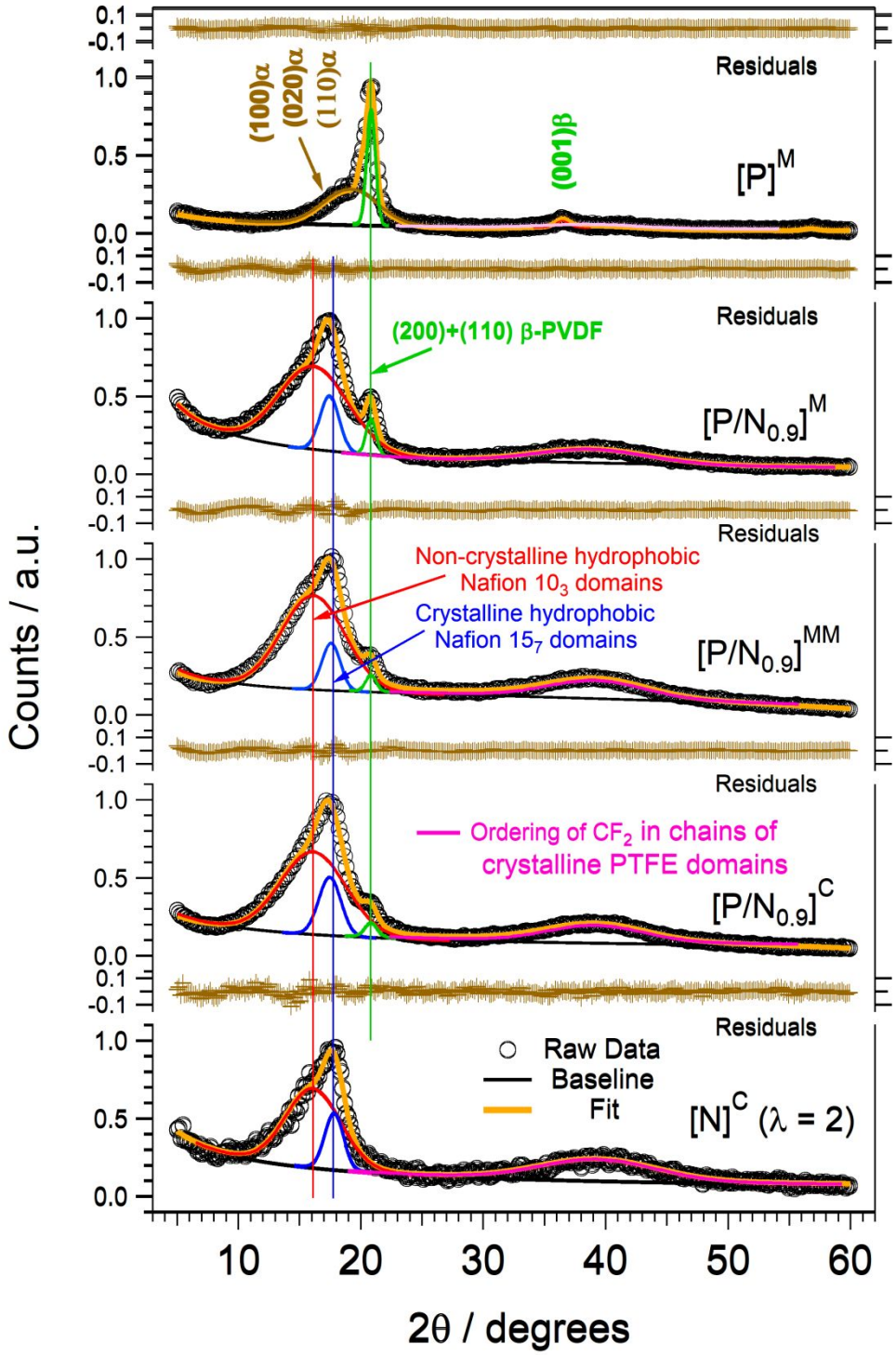


**Figure 9.** WAXD patterns of $[P/N_{0.9}]^X$ , $[P]^M$ and $[N]^C$ ($\lambda = 2$); $[P/N_{0.9}]^X$ are exposed to ambient atmosphere before the measurement and are thus considered *"wet"*.

Using the Scherrer formula [49], subtle conformational differences can be detected between $[P/N_{0.9}]^X$ membranes, that highlight the effect of the fabrication method upon the resulting structure. These results are summarized in Figure 10. The $15_7$ abundance in $[P/N_{0.9}]^X$ (X = M, MM, and C) is calculated to be lower than that present in $[N]^C$ ($\lambda = 2$). This is especially evident for X = M and MM (see Figure 10(a)). In order to maximize dipole-dipole interactions between PVDF and the PTFE backbone chains and possibly, to a lesser extent, the polar side chains of Nafion in $[P/N_{0.9}]^X$ (which govern the thermal properties observed by HR-TGA and TMDSC), the backbones of Nafion adopt a $2_1$ a conformation that is compatible with the repeating zig-zag motif of PVDF. The $15_7$ conformation (that is less compatible with PVDF) should decrease as the $2_1$ helical conformation (two monomeric units per helix turn) is preferentially adopted [50] and this is seen in Figure 10a. Unfortunately, there is no direct evidence of the $2_1$ helical conformation in WAXD patterns of $[P/N_{0.9}]^X$ because such a helical conformation only appears at the interface between Nafion and PVDF and does not form separate domains of a large enough size to be detected by WAXD. The size of $15_7$ and $10_3$ domains, as shown in Figure 10b, remain largely constant across all samples and are comparable to those found in the sample $[N]^C$ ($\lambda = 2$), suggesting that the size of $15_7$ and $10_3$ domains are independent on the sample type [40, 41]. This agrees with the TMDSC data (see Section 3.3), where the temperatures of the melting events (I, III and IV) for wet $[P/N_{0.9}]^X$ are all similar to each other and also equal to that of $[N]^C$ ($\lambda = 2$). It should also be noted that the weight percentage of β-phase PVDF in $[P/N_{0.9}]^X$ samples (shown in Figure 10(a)) is of the same order of magnitude as the crystallinity percentages determined in the same samples by means of TMDSC (see Section 3.3). This result confirms that the crystalline domains of PVDF mainly consist of the polymer's β-phase.

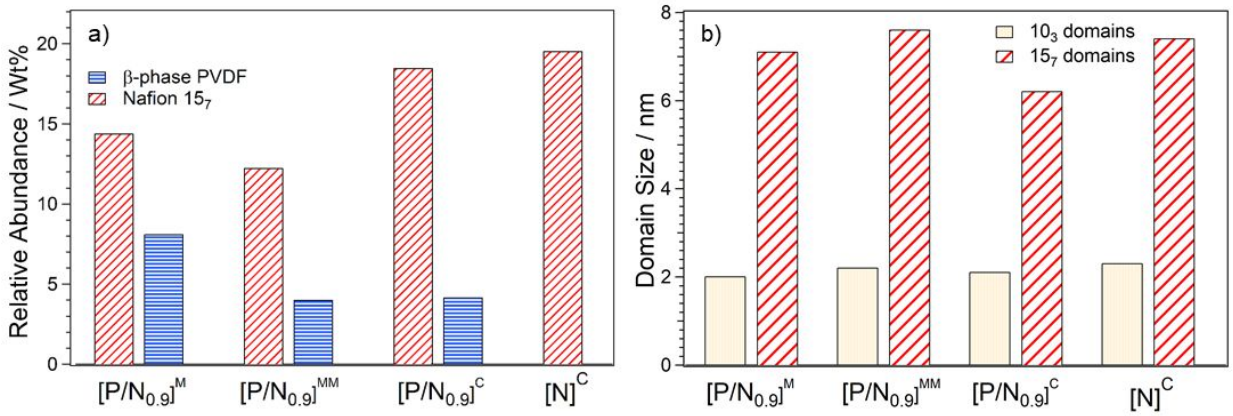


**Figure 10.** The effect of fabrication method on the relative abundance of β-phase PVDF (a), $15_7$ and $10_3$, and also on domain sizes in wet $[P/N_{0.9}]^X$ and $[N]^C$ ($\lambda = 2$) (b) (relative abundance calculated from ref. [50]). Samples have been exposed to an ambient atmosphere after water equilibration and are therefore deemed to be *"wet"*.

*3.5. Attenuated Total Reflectance - Fourier Transform Infra Red Spectroscopy (ATR-FTIR)*

ATR-FTIR spectra for $[P]^M$ and $[P]^{MM}$ is shown in Figure 11. The spectrum of $[P]^M$ is dominated by bands associated with β-phase PVDF, which is in good agreement with the WAXD data [20, 22, 28, 37, 47]. Following the heat-induced conversion of fiber mat $[P]^M$ to membrane $[P]^{MM}$, significant changes are observed in the ATR-FTIR spectrum. Bands attributed to α-phase PVDF grow at the expense of β-phase PVDF. Indeed, in $[P]^{MM}$, the α-phase is now the dominating polymorph, at 71% abundance (the relative abundance was obtained using the equation shown in Equation SI-3). This polymorphic inversion of the PVDF highlights the thermal sensitivity of the β-phase.

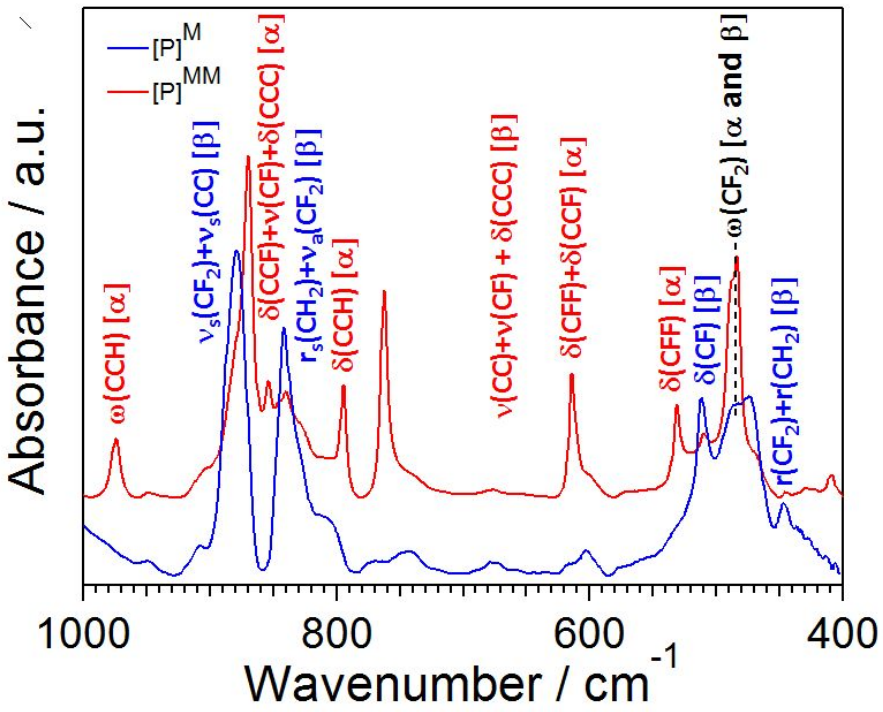


**Figure 11.** ATR-FTIR spectra for $[P]^{M}$ and $[P]^{MM}$ in the region 400 ÷ 1000 $cm^{-1}$ with selected bands corresponding to α- and β-phase PVDF [20, 22, 28, 37, 47]. Full spectra and band assignment tables can be found in the supplementary information (see Figure SI-4, Table SI-5 and Table SI-6).

The ATR-FTIR spectra of $[P/N_{0.9}]^{M}$, $[P/N_{0.9}]^{MM}$, $[P/N_{0.9}]^{C}$ (see Figure 12) are dominated, as expected, by Nafion which is the dominant component in these samples. However, diagnostic bands of β-phase PVDF can be observed for all spectra (regardless of hydration), centered at 838, 878 and 1402 $cm^{-1}$ and are assigned respectively to $r(CH_2) + \nu_a(CF_2)$, $\nu_s(CF_2) + \nu_s(CC)$ and $\omega(CH_2) - \nu_a(CC)$ motions. Bands corresponding to α-phase PVDF are not readily observed. The absence of α-phase PVDF in the spectrum of $[P/N_{0.9}]^{MM}$ is particularly surprising given that this sample undergoes a treatment at elevated temperatures (*i.e.*, hot-pressing, see Section 2.1.2) which encourages the β → α phase transition. It would appear that the interchain interactions (*"reciprocal*

*templating"* effect) between PVDF and the PTFE backbone of Nafion raises the thermal stability of the β-phase in $[P/N_{0.9}]^X$ (X = M and MM), thus locking in this conformation even at high temperatures. For dry $[P/N_{0.9}]^X$ (X = M, MM and C), the $–SO_3H$ fixed charge groups of Nafion are present in both: (i) the undissociated form, as revealed by the $\nu_s(SO_3H)$ mode observed at 1410 $cm^{-1}$ and (ii) the dissociated state, as highlighted by the $\nu_s(SO_3^-)$ vibration detected at 1062 $cm^{-1}$. These features are very similar to those observed for $[N]^C$ (λ = 0) [19, 22, 28, 51, 52]. The mode of β-PVDF assigned to $\omega(CH_2)$ - $\nu_a(CC)$ also contributes to the band observed at 1410 $cm^{-1}$ (see Table SI-6 in the Supporting Information). For $[N]^C$ (λ = 2), all sulfonic acid groups are rendered dissociated, with the loss of the 1410 $cm^{-1}$ band (see Figure 12). For wet $[P/N_{0.9}]^X$, however, the band at 1410 $cm^{-1}$ does not disappear completely. In wet $[P/N_{0.9}]^X$ this band is attributed to the β-PVDF mode assigned to $\omega(CH_2)$ - $\nu_a(CC)$ (see above and Table SI-6). It should also be noted that the broad peaks observed in the ATR-FTIR spectrum of $[N]^C$ (λ = 22) and centered at *ca.* 1700 $cm^{-1}$ (see Figure 12) and 3400 $cm^{-1}$ (see the additional ATR-FTIR spectra in Figure SI-8), that are associated with water and water aggregates, show a very weak intensity in the spectra of wet $[P/N_{0.9}]^X$. This suggests that the water environment in the composite materials $[P/N_{0.9}]^X$ (X = M, MM and C) is different from that of water in $[N]^C$ (λ = 22). This is likely the result of the *"reciprocal templating"* effect of the PVDF, that imposes a conformational constraint on the PTFE Nafion backbone. This constraint results in sulfonate fixed charge groups adopting a very different conformation with respect to those in $[N]^C$ (λ = 22), altering dramatically their water uptake environment. Indeed, in accordance with the results obtained by HR-TGA (see Section 3.2) and TMDSC (see Section 3.3), the ATR-FTIR spectra shown in Figure 12 and Figure SI-8 reveal that even at full hydration the water uptake of the composite materials $[P/N_{0.9}]^X$ (X = M, MM and C)

is dramatically lower than that of the reference solution cast Nafion film ($[N]^C$). This is a consequence of the interactions between PVDF and Nafion components.

Another important difference between $[P/N_{0.9}]^X$ and $[N]^C$ in both the dry and the wet state is the intensity and shape of the bands located in the region 1112 ÷ 1351 $cm^{-1}$. For $[N]^C$, these bands represent composite signals associated with the symmetric stretching ($\nu_s$), anti-symmetric stretching ($\nu_a$), rocking (r) and bending bands ($\delta$) of differing helical conformations of Nafion's PTFE backbone chains. Thus, spectral differences suggest that the conformation of Nafion in $[P/N_{0.9}]^X$ and $[N]^C$ is different. Indeed, the presence of *"guests"* within the Nafion macromolecular matrix is known to modulate the relative abundance of the various PTFE helical conformations [14, 17, 29, 52, 53]. Given that PVDF adopts a $2_1$ helical conformation, in order to maximize interchain dipole-dipole interactions, the PTFE backbone chains of Nafion likely adopt a complementary $2_1$ conformation. This $2_1$ contribution is reflected by the band intensity differences for $[P/N_{0.9}]^X$ with respect to $[N]^C$. This result is in agreement with the WAXD data, that suggests different contributions of PTFE helical conformations [28, 42-44, 46, 49, 52].

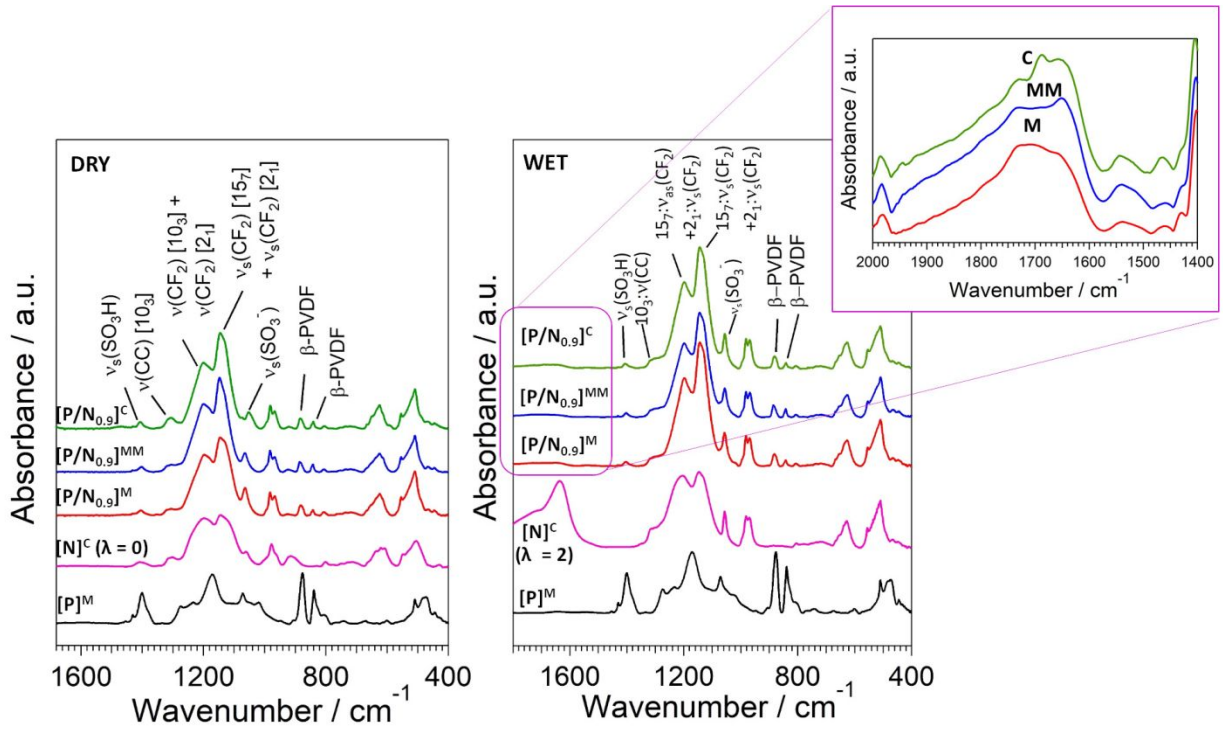


**Figure 12.** ATR-FTIR spectra in the region 400 ÷ 1800 $cm^{-1}$ of $[P/N_{0.9}]^{M}$ (red), $[P/N_{0.9}]^{MM}$ (blue), $[P/N_{0.9}]^{C}$ (green), $[P]^{M}$ (black) and $[N]^{C}$ ($\lambda = 0/2$) (pink)in the dry (left) and wet (right) states. The very strong peak observed at 876 $cm^{-1}$ corresponding to $\nu_s(CF_2) + \nu_s(CC)$ modes of PVDF is largely unaffected by fabrication method and/or hydration state and therefore all spectra are normalized to this peak. The inset magnifies the region 1400 ÷ 2000 $cm^{-1}$ of the spectra of the wet samples. Full spectra and data tables can be found in the Supplementary Information (see Figures SI-7, SI-8 and Table SI-9).

The effect of fabrication method on the conformation of the Nafion component in $[P/N_{0.9}]^{X}$ is further elaborated through the calculated difference spectra which are calculated by subtracting the normalized spectra of $[P]^{M}$ from the normalized spectra of $[P/N_{0.9}]^{X}$. As shown in Figure 13, there are noticeable variances between the difference spectra of $[P/N_{0.9}]^{X}$ materials in the dry state. These are attributed to differing helical contributions of the Nafion component, in particular,

differing $2_1$ conformational contributions [14]. Indeed, the $2_1$ contribution is calculated to be slightly higher for dry $[P/N_{0.9}]^M$ than dry $[P/N_{0.9}]^{MM}$ (see Figure SI-10 in the Supporting Information), suggesting that the hot-pressing step acts to reduce the ordering of perfluorinated chains within PTFE domains at the interface with PVDF. In the wet state, all $[P/N_{0.9}]^X$ spectra become congruent, implying that the conformational nature of Nafion is now identical in all composite samples. Upon hydration, the $2_1$ contribution is calculated to be equal for all $[P/N_{0.9}]^X$, implying that synergistic interactions between Nafion and PVDF are maintained despite being mediated in these wet materials by hydrogen bonding interactions due to water, as opposed to the interchain dipole-dipole interactions in dry samples, which involve PVDF and Nafion's backbone and possibly, to a lesser extent, the side chains of Nafion (the TMDSC results in Section 3.3 also suggest this conclusion).

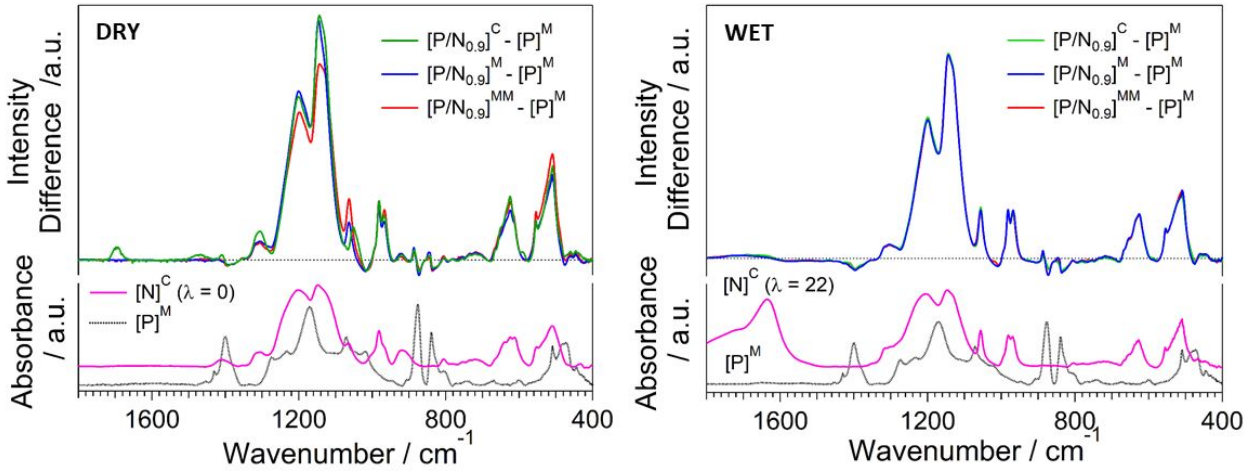


**Figure 13.** ATR-FTIR difference spectra for $[P/N_{0.9}]^X$ in the dry state (left) and in the wet state (right) with the corresponding $[P]^M$ and $[N]^C$ spectra shown below. The difference spectra are calculated by subtracting the normalized spectra of $[P]^M$ from the normalized spectra of $[P/N_{0.9}]^X$. The spectra of both $[P]^M$ and $[P/N_{0.9}]^X$ are normalized on the peak at 876 $cm^{-1}$ (see the Caption of Figure 12).

These results show that the TTT conformation of β-phase PVDF chains (see Figure 8) confers a complimentary $2_1$ conformation onto the PTFE backbone chains of Nafion. This ensures compatibility between the two types of polymer chains in the dry state via dipole-dipole interactions. In this conformation, the ethereal side groups of the Nafion component, with terminal sulfonic acid moieties, are pointing away from the backbone-backbone phases. It is this orientation of the sulfonic acid moieties that limits the water uptake in $[P/N_{0.9}]^X$ samples as suggested by HR-TGA (see Section 3.2). Interestingly, the $2_1$ PTFE helical conformation of Nafion's backbone is maintained in wet $[P/N_{0.9}]^X$ despite the fact that the water molecules disrupt the dipole-dipole interactions between polymer chains, replacing them with the uniform formation of equivalent hydrogen bonds (as suggested by TMDSC, see Section 3.3). The presence of these water molecules in wet $[P/N_{0.9}]^X$ materials at the interfaces between the Nafion and PVDF polymer components is confirmed by the bending mode at *ca.* 1550 $cm^{-1}$ (see the inset of Figure 12), which is assigned to $(H_2O)_2$ dimers with their lowest possible dipolar moment [19]. In [Nafion/$(SiO_2)_x$] composite membranes[18] this vibrational mode is detected at 1590 $cm^{-1}$. Instead, in the $[P/N_{0.9}]^X$ materials this mode is peaking at 1550 $cm^{-1}$, *i.e.*, it is shifted to lower wavenumbers by *ca.* 40 $cm^{-1}$. This demonstrates that in the $[P/N_{0.9}]^X$ materials the water dimers are experiencing an environment that is more hydrophobic than that of [Nafion/$(SiO_2)_x$]. This is easily explained if we consider that for the OH vibrational modes[54]: (i) a decrease in the OH stretching frequency by 50 $cm^{-1}$ corresponds to an increase in the interactions between OH groups by roughly 1 kcal/mol; and (ii) bending vibrations occur at energies that are at least one order of magnitude lower with respect to those of stretching vibrations. Taking all together, with respect to [Nafion/$(SiO_2)_x$] composite membranes[19] a shift towards lower frequencies of 40 $cm^{-1}$ in bending vibrations corresponds to an increase of

water dimer interactions of *ca.* 0.4784 kJ/mol, which is: (i) of the order of magnitude typical of van der Waals interactions; (ii) *ca.* one order of magnitude lower than that expected for a strengthening of interactions in stretching vibrations of hydrogen bonding. On this basis, the peak at 1550 $cm^{-1}$ is diagnostic to reveal that water dimers in the $[P/N_{0.9}]^X$ materials, with respect to $[Nafion/(SiO_2)_x]$ composite membranes[19], experience a more hydrophobic environment. This result is also in accordance with the difference in water uptake of $[Nafion/(SiO_2)_x]$ composite membranes and the blended fiber membranes in the present study. The presence of this interfacial water allows for the retention of the $2_1$ helical conformation, but also renders all Nafion components between $[P/N_{0.9}]^X$ members largely equivalent (see Figure 14).

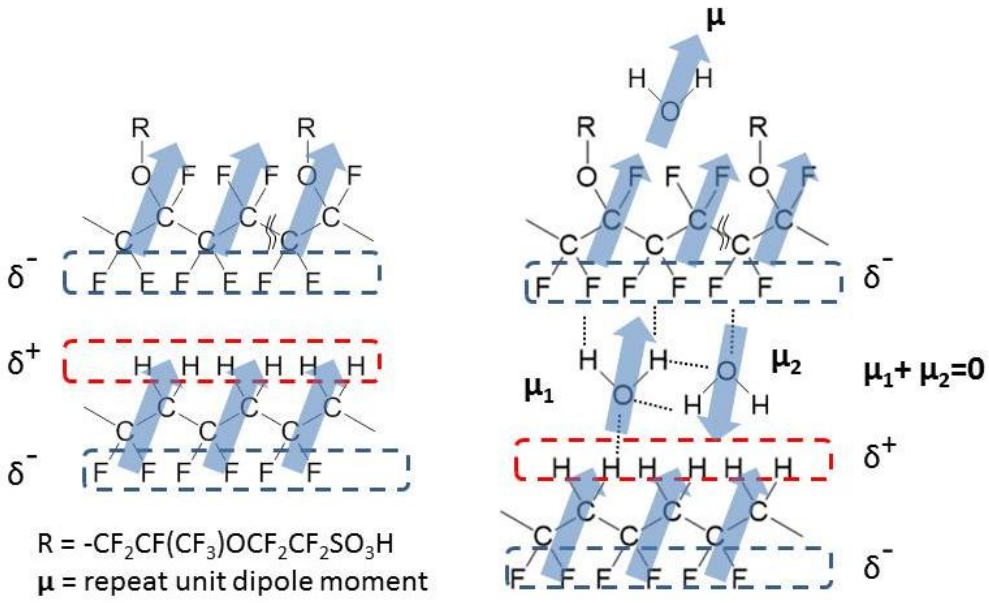


**Figure 14.** The dipole-dipole interactions between the conformational compatible TTT PVDF and the $2_1$ induced PTFE Nafion backbone in the dry state (left). The introduction of hydrogen bonding interactions in the wet state with $2_1$ retention (right). At the interface between PVDF and Nafion, it is hypothesized the presence of traces of $(H_2O)_2$ dimers [19].

## 4. Conclusions

A new type of polymer blend, obtained by electrospinning fibers of two immiscible polymers, *i.e.*, Nafion and polyvinylidene fluoride (PVDF), has been characterized experimentally using SEM, TEM, TGA, TMDSC, WAXD, and ATR-FTIR. The internal morphology of nanofibers (~500 nm in diameter) is unique and unlike a normal polymer blend, with individual phase-separated and randomly distributed fibrils of Nafion and PVDF (~ 1 nm in diameter) that are bundled together and aligned in the fiber axis direction. This internal morphology is retained when fiber mats are hot-pressed into dense films. The properties of the electrospun blended fibers are highly unusual, where each polymer component influences the thermal and structural behavior of the other (this phenomenon is herein termed as *"reciprocal templating"*), and the resulting composite mats and membranes demonstrate attributes that are not observed for either pure PVDF or pure Nafion. The properties and structural features of $[P/N_{0.9}]^X$ materials obtained by electrospinning, where P = PVDF, N = Nafion, and X = M (fiber mat) or MM (membrane obtained from mat by hot-pressing) are contrasted with solution-cast PVDF/Nafion films ($[P/N_{0.9}]^C$) for a mixture of Nafion 1100 (90 wt%) and PVDF (10 wt%). HR-TGA investigations show that the presence of PVDF modulates the thermal properties of the electrospun composite materials (especially in the dry state). The interactions between PVDF and PTFE backbone chains of the Nafion component also restricts the water uptake of the composite materials in such a way that the Nafion component in wet $[P/N_{0.9}]^X$ behaves like $[N]^C$ ($\lambda = 2$), with a dramatically lower water uptake. TMDSC reveals that: (a) the melting transitions of the Nafion component in dry $[P/N_{0.9}]^X$ are significantly influenced by the secondary structure of PTFE and PVDF domains, the PTFE-PVDF interactions, and the fiber mat processing protocol; and (b) the TTT structure of β-PVDF significantly affects the $T_{\alpha 1}$, $T_{\alpha 2}$ and $T_\beta$ thermal transitions of the hydrophobic PTFE domains of supported Nafion. Vibrational analysis,

in agreement with WAXD shows that: (a) the β-phase of PVDF with the TTT secondary structure is retained upon conversion of the composite mat $[P/N_{0.9}]^{M}$ to dense composite membrane $[P/N_{0.9}]^{MM}$ upon hot-pressing; and (b) in PTFE domains, the β-PVDF/Nafion interactions modulate the distribution of perfluorinated chains with that of the complimentary $2_1$ helical conformation preferentially adopted. The results of *"reciprocal templating"* in the samples presented in this work can be summarized as follows: (i) the PTFE backbone chains and the structural rearrangement of the side chains of Nafion influence the structure of PVDF, stabilizing the β-phase; (ii) PVDF imparts conformational preference onto the Nafion backbone chains favoring a complimentary $2_1$ helical backbone conformation and promoting interactions between side chains, thus inhibiting the water uptake. *"Reciprocal templating"* in electrospun fibers may not be unique to Nafion and PVDF. Therefore, we are convinced that the procedure described here represents a new method of creating multi-component polymer materials with an innovative morphology and structure.

**Acknowledgements**

Work performed at Vanderbilt University was supported by the National Science Foundation (Grant no. EFRI-1038234) and the Advanced Research Projects Agency-Energy (ARPA-E) of the U.S. Department of Energy (Contract no. DE-AC02-05CH1123). The work carried out at the University of Padova was supported by the project *"Novel Multilayered and Micro-Machined Electrode Nano-Architectures for Electrocatalytic Applications (Fuel Cells and Electrolyzers)"*, (protocol 2017YH9MRK) of the Italian MIUR, financed in the framework of *"PRIN 2017"* call.

**References**


1. K. A. Mauritz and R. B. Moore, *Chemical Reviews*, 2004, **104**, 4535-4586.
2. P. Arora and Z. Zhang, *Chemical Reviews*, 2004, **104**, 4419-4462.
3. Z. Mai, H. Zhang, X. Li, S. Xiao and H. Zhang, *Journal of Power Sources*, 2011, **196**, 5737-5741.
4. K. Heiji, *Japanese Journal of Applied Physics*, 1969, **8**, 975.
5. A. Vinogradov and F. Holloway, *Ferroelectrics*, 1999, **226**, 169-181.
6. M.-K. Song, Y.-T. Kim, J. M. Fenton, H. R. Kunz and H.-W. Rhee, *Journal of Power Sources*, 2003, **117**, 14-21.
7. H. J. Kim, H. J. Kim, Y. G. Shul and H. S. Han, *Journal of Power Sources*, 2004, **135**, 66-71.
8. S. W. Choi, Y. Z. Fu, Y. R. Ahn, S. M. Jo and A. Manthiram, *Journal of Power Sources*, 2008, **180**, 167-171.
9. J. O. Lin, M.; Fenton, J.; Kunz, H.; Koberstein, J.; Cutlip, M., *Journal of Applied Polymer Science*, 1998, **70**, 8.
10. J. W. Park, R. Wycisk and P. N. Pintauro, *Journal of Membrane Science*, 2015, **490**, 103-112.
11. J. W. Park, R.; Lin, G.; Van Nguyen, T.; Pintauro, P. , *Electrochemical Society Meeting Abstract*, 2015, **MA2015**, 1.
12. J. Woo Park, R. Wycisk, G. Lin, P. Ying Chong, D. Powers, T. Van Nguyen, R. P. Dowd Jr and P. N. Pintauro, *Journal of Membrane Science*, 2017, **541**, 85-92.
13. G. Nawn, K. Vezzù, E. Negro, G. Crivellaro, G. Cavinato, J. W. Park, R. Wycisk, P. N. Pintauro and V. Di Noto, *Physical Chemistry Chemical Physics*, in process.

14. E. Negro, M. Vittadello, K. Vezzù, S. J. Paddison and V. Di Noto, *Solid State Ionics*, 2013, **252**, 84-92.

15. D. W. M. Hofmann, L. Kuleshova, B. D'Aguanno, V. D. Noto, E. Negro, F. Conti and M. Vittadello, *Journal of Physical Chemistry B*, 2009, **113**, 632-639.

16. G. Alberti, R. Narducci and M. Sganappa, *Journal of Power Sources*, 2008, **178**, 575-583.

17. V. Di Noto, N. Boaretto, E. Negro and G. Pace, *Journal of Power Sources*, 2010, **195**, 7734-7742.

18. L. F. Malmonge and L. H. C. Mattoso, *Polymer*, 2000, **41**, 8387-8391.

19. V. Di Noto, R. Gliubizzi, E. Negro and G. Pace, *The Journal of Physical Chemistry B*, 2006, **110**, 24972-24986.

20. S. H. de Almeida and Y. Kawano, *Journal of Thermal Analysis and Calorimetry*, 1999, **58**, 569-577.

21. X. Zhao, S. Chen, J. Zhang, W. Zhang and X. Wang, *Journal of Crystal Growth*, 2011, **328**, 74-80.

22. V. D. Noto, M. Piga, G. A. Giffin, S. Lavina, E. S. Smotkin, J.-Y. Sanchez and C. Iojoiu, *The Journal of Physical Chemistry C*, 2012, **116**, 1361-1369.

23. V. Di Noto, M. Piga, G. A. Giffin, K. Vezzù and T. A. Zawodzinski, *Journal of the American Chemical Society*, 2012, **134**, 19099-19107.

24. G. A. Giffin, M. Piga, S. Lavina, M. A. Navarra, A. D'Epifanio, B. Scrosati and V. Di Noto, *Journal of Power Sources*, 2012, **198**, 66-75.

25. V. P. Di Noto, M.; Negro, E.; Pace, P.; Lavina, S., *ECS Transactions*, 2008, **16**, 11.

26. V. Di Noto, G. A. Giffin, K. Vezzù, G. Nawn, F. Bertasi, T. H. Tsai, A. M. Maes, S. Seifert, E. B. Coughlin and A. M. Herring, *Physical Chemistry Chemical Physics*, 2015, **17**, 31125-31139.

27. K. Vezzù, A. M. Maes, F. Bertasi, A. R. Motz, T. H. Tsai, E. B. Coughlin, A. M. Herring and V. Di Noto, *Journal of the American Chemical Society*, 2018, **140**, 1372-1384.

28. V. Di Noto, M. Piga, S. Lavina, E. Negro, K. Yoshida, R. Ito and T. Furukawa, *Electrochimica Acta*, 2010, **55**, 1431-1444.

29. E. S. Clark, *Polymer*, 1999, **40**, 4659-4665.

30. M. Kobayashi, K. Tashiro and H. Tadokoro, *Macromolecules*, 1975, **8**, 158-171.

31. A. B. da Silva, C. Wisniewski, J. V. A. Esteves and R. Gregorio, *Journal of Materials Science*, 2010, **45**, 4206-4215.

32. Y. Yang, A. Centrone, L. Chen, F. Simeon, T. Alan Hatton and G. C. Rutledge, *Carbon*, 2011, **49**, 3395-3403.

33. L. Yu and P. Cebe, *Polymer*, 2009, **50**, 2133-2141.

34. S. W. Choi, J. R. Kim, Y. R. Ahn, S. M. Jo and E. J. Cairns, *Chemistry of Materials*, 2007, **19**, 104-115.

35. R. Gregorio, *Journal of Applied Polymer Science*, 2006, **100**, 3272-3279.

36. R. Gregorio and E. M. Ueno, *Journal of Materials Science*, 1999, **34**, 4489-4500.

37. D. K. Das-Gupta and K. Doughty, *Journal of Applied Physics*, 1978, **49**, 4601-4603.

38. B. A. Newman, C. H. Yoon, K. D. Pae and J. I. Scheinbeim, *Journal of Applied Physics*, 1979, **50**, 6095-6100.

39. C. W. Bunn and E. R. Howells, *Nature*, 1954, **174**, 549.

40. C. F. Nørgaard, U. G. Nielsen and E. M. Skou, *Solid State Ionics*, 2012, **213**, 76-82.

41. M. Fujimura, T. Hashimoto and H. Kawai, *Macromolecules*, 1981, **14**, 1309-1315.

42. G. Masetti, F. Cabassi, G. Morelli and G. Zerbi, *Macromolecules*, 1973, **6**, 700-707.

43. G. Zerbi and M. Sacchi, *Macromolecules*, 1973, **6**, 692-699.

44. L. Piseri, B. M. Powell and G. Dolling, *The Journal of Chemical Physics*, 1973, **58**, 158-171.

45. K. Tashiro, M. Kobayashi and H. Tadokoro, *Macromolecules*, 1981, **14**, 1757-1764.

46. M. J. Hannon, F. J. Boerio and J. L. Koenig, *The Journal of Chemical Physics*, 1969, **50**, 2829-2836.

47. B. E. R. N. G. McCrum, and G. Williams, *Anelastic and Dielectric Effects on Polymeric Solids*, John Wiley & Sons, London, 1967.

48. P. M. Nallasamy, S., *Industrial Journal Pure and Applied Physics*, 2005, **43**, 8.

49. H. A. Klug, L. , *X-Ray Diffraction Procedures: For Polycrystalline and Materials*, John Wiley & Sons, New York, 1974.

50. Y. F. Gnanou, M., *Organic and Physical Chemistry of Polymers*, John Wiley & Sons, New York, 2008.

51. V. Di Noto, R. Gliubizzi, E. Negro, M. Vittadello and G. Pace, *Electrochimica Acta*, 2007, **53**, 1618-1627.

52. V. Di Noto, M. Piga, L. Piga, S. Polizzi and E. Negro, *Journal of Power Sources*, 2008, **178**, 561-574.

53. M. Vittadello, E. Negro, S. Lavina, G. Pace, A. Safari and V. D. Noto, *The Journal of Physical Chemistry B*, 2008, **112**, 16590-16600.

54. V. Di Noto, D. Longo and V. Münchow, *Journal of Physical Chemistry B*, 1999, **103**, 2636-2646.

Graphical Abstract